Effects of intense strain on flame structure and NOx generation in turbulent counterflow lean-premixed hydrogen flames

Fathi, Mohamad; Hickel, Stefan; Doan, Nguyen Anh Khoa; Langella, Ivan

DOI
10.1016/j.combustflame.2025.114459

Publication date
2025

Document Version
Final published version

Published in
Combustion and Flame

Citation (APA)
Fathi, M., Hickel, S., Doan, N. A. K., & Langella, I. (2025). Effects of intense strain on flame structure and NOx generation in turbulent counterflow lean-premixed hydrogen flames. *Combustion and Flame*, *282*, Article 114459. https://doi.org/10.1016/j.combustflame.2025.114459

Combustion and Flame 282 (2025) 114459

Contents lists available at ScienceDirect

Combustion and Flame

journal homepage: www.sciencedirect.com/journal/combustion-and-flame

Effects of intense strain on flame structure and NOx generation in turbulent counterflow lean-premixed hydrogen flames

Mohamad Fathi *, Stefan Hickel, Nguyen Anh Khoa Doan, Ivan Langella

Faculty of Aerospace Engineering, Delft University of Technology, Kluyverweg 1, Delft, 2629 HS, The Netherlands

ARTICLE INFO

Keywords:
Turbulent counterflows
Lean premixed flames
Hydrogen combustion
Highly strained flames
NOx generation
DNS

ABSTRACT

Direct numerical simulations (DNS) are conducted for reactants-to-products counterflow configurations at turbulent conditions to understand how strain affects the structure and NOx emissions of lean premixed hydrogen flames. Two nominal equivalence ratio conditions, 0.5 and 0.7, are investigated. Under unstretched conditions, the Markstein length is negative for the former and slightly positive for the latter, indicating distinct responses of heat release rate and flame consumption speed to strain in each case. For each equivalence ratio condition, three levels of applied strain rate are considered, resulting in a total of six DNS. Results indicate that overall NOx emissions decrease with increasing strain at turbulent conditions, consistent with recent results for laminar conditions presented in Porcarelli et al. (2024). However, the relative decrease of NOx with strain is faster under turbulent conditions because turbulent mixing limits the occurrence of super-adiabatic temperatures. Moreover, the decrease of NOx is strongly correlated only to the mean applied tangential strain rate, while local fluctuations of strain due to vortices exhibit more stochastic behaviour. The detailed analysis presented in this article indicates that the applied strain can be used to substantially decrease NOx emissions in premixed hydrogen flames under practical conditions.

Novelty and Significance statement:

This work examines for the first time in detail the coupled effects of strain and turbulence in hydrogen flames, for various conditions spanning different signs of the Markstein length and increasing applied strain levels. In particular, it clarifies the different roles of applied strain, turbulence-driven strain, and curvature on both flame structure and NOx generation. Results further show for the first time that both in-flame and post-flame NOx can be suppressed at high strain levels under turbulent conditions. This result is of paramount importance as it implies that NOx can be suppressed at combustor-relevant conditions by straining the flame.

1. Introduction

Hydrogen is increasingly popular as a promising energy carrier mainly due to its zero carbon emissions, high energy density, and potential for production from renewable resources [1]. However, its relatively high adiabatic flame temperature as compared to that of hydrocarbon fuels implies that significant amounts of nitrogen oxides (NOx) can be generated when burned with air. Generally, NOx emissions can be generated inside and after the flame. The post-flame NOx is produced mainly through the oxidation of nitrogen in the air at high temperatures, typically above 1700 K, and its formation depends directly on temperature and residence time. In high-temperature energy systems like gas turbines, managing post-flame NOx often requires reducing residence time by adopting more compact designs. On the other hand, flame-generated NOx forms directly within the flame through rapid reactions involving radicals from the oxyhydrogen pool in the reaction zone. Unlike post-flame NOx, in-flame NOx is not influenced by the overall residence time or the size of the combustor [2,3].

As compared to other fuels, the high reactivity and heating value of hydrogen allows operations under lean-premixed combustion conditions, which can significantly reduce post-flame NOx formation by lowering the adiabatic flame temperature. However, lean-burn systems present practical challenges, such as flame blow-off, flashback, and thermoacoustic instabilities, which limit the viability of lean premixed combustion as a standalone solution [4,5]. These challenges can be exacerbated in the case of hydrogen flames due to the faster diffusion of hydrogen as compared to other species and heat, which can lead respectively to local enrichment and the occurrence of thermodiffusive instabilities, which will increase the flame speed [6–9]. Moreover, despite lean conditions, NOx can persist in the hydrogen flame itself due to elevated concentrations of intermediate radicals such as H and

---

* Correspondence to: Faculty of Aerospace Engineering, TU Delft, Kluyverweg 1, Delft, 2629 HS, The Netherlands.
E-mail address: m.fathi@tudelft.nl (M. Fathi).

https://doi.org/10.1016/j.combustflame.2025.114459
Received 27 March 2025; Received in revised form 4 September 2025; Accepted 4 September 2025

OH in the reaction zone [10,11]. To further mitigate both post-flame and in-flame NOx emissions, several techniques have been explored, such as catalytic reactions [12], microinjection [13], water or steam injection [14], and multiple-swirl injection [15]. In the latter, a key role was observed to be played by flame tangential strain rate (FTS), which increases with swirl number and shear stress [16].

Compared to conventional fuels, hydrogen can also stabilize and burn effectively in regions of very high strain [17,18], making FTS-based methods particularly effective in NOx reduction for lean premixed hydrogen flames [19–21]. Sufficiently high levels of (positive) strain were also shown in asymptotic analyses [6] to prevent the onset of thermodiffusive instabilities, thus limiting the flame surface growth in hydrogen flames. However, the dynamics of NOx suppression through straining, particularly under turbulent conditions, are not yet understood. The counterflow configuration has been widely used to study the direct effects of strain on flames. In particular, recent research [20] has indicated that NOx is suppressed by strain in reactants-to-products laminar lean premixed flames, mainly due to a redistribution of OH radicals within the flame region. Nevertheless, whether this suppression would manifest also at turbulent conditions, where a range of turbulence and combustion scales are present, is still unclear. In this regard, direct numerical simulation (DNS) can offer valuable insights into turbulent flame behaviour by providing high-resolution data on the complex interactions between flame and flow dynamics. Turbulent counterflow flames in particular, like their laminar counterparts [20], provide in this regard an ideal framework for analysing the relation between NOx formation and applied strain. However, performing DNS of turbulent counterflow flames presents significant challenges [22,23].

For DNS to accurately capture NOx generated inside and after the flame, it must incorporate a detailed NOx reaction mechanism. Such reaction mechanisms should contain three key pathways: the Zeldovich mechanism, the N_2O intermediate pathway, and the diazenyl radical (NNH) route [24,25]. More recently, Wen et al. [26,27] investigated the effect of flame curvature on NOx formation pathways in freely propagating lean premixed hydrogen flames with an equivalence ratio of 0.4. At atmospheric pressure, their DNS results show that more than 90 % of NO is produced through the NNH pathway in positively curved flame regions, where H-radicals accumulate, while at a pressure of 8 bar the N_2O pathway plays a more crucial role. Nevertheless, the main focus of these analyses was on the effect of curvature, and further analysis is necessary to examine NOx formation in highly strained turbulent hydrogen flames.

The objective of the present study is to investigate how hydrogen flame straining influences both in-flame and post-flame NOx formation, providing a deeper understanding of NOx suppression mechanisms under turbulent and lean conditions. To this end, we have conducted a series of DNS studies for turbulent fresh-to-burnt gas counterflow flames, in which a laminar stream of hot combustion products is introduced from one side, while a turbulent stream of cold reactants enters from the opposite side. The DNS solves the fully conservative formulation of the multicomponent compressible Navier–Stokes equations, including differential diffusion and variable thermo-transport properties in the context of finite-rate chemistry using a detailed NOx reaction mechanism. The bulk strain rate applied to the hydrogen flame is varied by adjusting the inflow velocity of the laminar burnt-gases stream only so as to preserve the turbulence characteristics. Three levels of bulk strain have been considered: 2000, 3000, and 5000 s^{-1}. The simulations are conducted for two lean premixed flames with equivalence ratios of 0.5 and 0.7. The selected equivalence ratios allow to compare the effect of strain on NOx at conditions where the Markstein length is about zero ($\phi = 0.7$) and negative ($\phi = 0.5$) [28]. A negative Markstein length, other than implying that the flame consumption speed will increase with positive stretch, was in fact also observed for laminar hydrogen counterflow flames to slow down the effect of NOx suppression [20]. Therefore, its analysis serves to provide further insight into the coupled effects of differential diffusion and strain in turbulent conditions.

The structure of this paper is as follows. Section 2 addresses the numerical and physical models used. Section 3 describes the configuration and conditions of the test cases. Section 4 presents the results, starting from an analysis of the flame structures in physical and progress variable space, followed by a detailed analysis of the NOx production mechanisms. Section 5 provides conclusions and implications for future research.

2. Numerical methods

The reacting compressible Navier–Stokes equations with variable thermotransport properties and finite-rate chemistry are solved using the finite-volume DNS code INCA [29–33]. The physical and numerical models used for the present study are described in the Supplementary Material.

2.1. Discretization methods

We simulate counterflow flames in a hexahedral domain on a uniform Cartesian mesh. The mesh resolution is chosen based on the grid sensitivity study discussed in the Supplementary Material. All calculations are performed using a second-order Strang splitting scheme [34] to decouple the source terms of the stiff reaction from the Navier–Stokes equations. The isolated reaction terms result in a set of stiff ordinary differential equations (ODEs), which are solved with the fast explicit time integration method ERENA [35]. ERENA is constructed on the basis of the quasi-steady-state (QSS) method and a general formula that ensures the conservation of mass in its substeps. In this study, the ERENA error threshold is set to 10^{-9} and the final result is renormalized to ensure exact mass conservation.

The mass, momentum, and energy transport equations are discretized in space with a finite-volume scheme. The viscous fluxes are discretized using second-order central differences, and the inviscid fluxes are discretized using a high-order non-linear reconstruction scheme [36]. The van Albada limiter is applied to the mass and energy fluxes to ensure positivity of the mass fractions and the internal energy. The method ensures oscillation-free pressure–velocity coupling through an approximate solution of the compressible Riemann problem that is consistent with incompressible turbulence theory in the low-Mach limit [36]. Time marching is performed using an explicit third-order Runge–Kutta scheme [37] and the time-step size is dynamically adjusted so that CFL = 1.

2.2. Reaction mechanism

NOx production in hydrogen flames occurs via three pathways: the thermal Zeldovich mechanism, the N_2O intermediate pathway, and the secondary route through diazenyl radicals (NNH). Thermal formation of NOx is primarily determined by temperature due to the high activation energy of its initial reaction. In contrast, the N_2O intermediate pathway is almost temperature independent, as it is driven by a third-body reaction with low activation energy. The NNH pathway is also promoted in the flame front and is controlled by O and H radicals. These routes are linked through intermediate radicals and might influence each other. To address all these pathways, the reduced mechanism proposed by Capurso et al. [24] is used. From a modelling perspective, the kinetics of hydrogen combustion is well studied and forms submechanisms within the chemical kinetics of hydrocarbons. To balance accuracy with computational efficiency in the DNS, the Capurso mechanism for NOx is coupled with the skeletal mechanism proposed by Sanchez and Williams [38] for hydrogen combustion. The overall resulting mechanism sums up to 15 species and 37 elementary reaction steps. It is provided in the Cantera and Chemkin formats as Supplementary Material.

2.3. Characteristic boundary conditions

To prevent spurious wave reflections and ensure numerical stability in the presence of turbulent eddies crossing the domain boundaries of the counterflow configuration, characteristic-based non-reflecting boundary conditions (NSCBC) are employed. This approach solves a system of equations in a layer of ghost cells surrounding the computational domain to track the propagation of acoustic, vorticity, and species-entropy waves. Each wave strength is composed of normal and tangential contributions, determined from local flow variables such as pressure, density, velocity components, temperature, and species mass fractions.

At subsonic outlet boundaries, entropy and vorticity waves, as well as one acoustic wave, naturally leave the domain, while the incoming acoustic wave is estimated based on the sign of the normal velocity component and the deviation from a target outlet pressure. Pressure relaxation is introduced using a damping term involving a characteristic length scale and reference Mach number.

At subsonic inlets, all waves except one acoustic wave enter the domain. Incoming vorticity waves are adjusted according to differences between the target and actual tangential velocities, while entropy and acoustic waves are controlled via relaxation terms involving normal velocity, temperature, and species composition. The reader can find further details in the Supplementary Material.

2.4. Species equations and differential diffusion

The DNS code INCA solves the discretized equations for mass, momentum, total internal energy and species mass fractions. The full set of governing equations and formulations is provided in the Supplementary Material. Here only details for the species equation is provided. The transport equation for a single species is:

$$\partial_t(\rho Y_i) + \nabla \cdot \left(\rho Y_i \mathbf{u}\right) = \nabla \cdot \mathbf{j}_i + \dot{\omega}_i, \tag{1}$$

where ρ is the mixture density, $\mathbf{u}$ is the velocity vector, Y_i indicates the mass fraction of species i, $\mathbf{j}_i$ is its diffusive mass flux vector and $\dot{\omega}_i$ is its net mass production rate. The mass diffusion $\mathbf{j}_i$ is modelled with a mixture-average formulation with an extra term to ensure mass conservation,

$$\mathbf{j}_i = \rho D_i \nabla Y_i - Y_i \sum_{j=1}^{\mathrm{N}} \rho D_j \nabla Y_j. \tag{2}$$

The required effective binary diffusion coefficient between species i and the bulk mixture, D_i, is estimated from the thermal conductivity λ, the density ρ, and the specific heat capacity c_p as $D_i = \lambda/(\rho c_p Le_i)$, where the Lewis number of species i, Le_i, is assumed to be spatially homogeneous. Dufour and Soret effects are neglected in the present treatment. While thermodiffusion was shown to influence both Lewis number effect [39] and preferential diffusion [28] in laminar conditions, these works also indicate that it does not affect the overall trends in terms of emissions and flame structure interplay with strain. Since turbulence is expected to weaken the Soret effect [40], the latter was for simplicity neglected, as its application in the context of the mixture averaged model used in our work would require further modelling, which would increase uncertainty and computational cost.

3. Case setup and configurations

Direct Numerical Simulations (DNS) are performed for turbulent lean premixed hydrogen flames in a three-dimensional reactants-to-products counterflow configuration. The computational domain consists of a rectangular parallelepiped with dimensions 12 × 4 × 3 mm, as illustrated in Fig. 1. Two equivalence ratios of 0.5 and 0.7 are considered. The domain size in terms of the thermal unstretched flame thickness is about 30 × 10 × 7.5 and 36 × 12 × 9 for the equivalence ratios of 0.5 and 0.7, respectively, which is similar to that in [41,42]. It should be noted that the turbulent counterflow flames examined here do not exhibit the typical growth of thermodiffusively unstable laminar flames due to the stabilizing effect of applied strain [6] and the fact that the time scales of turbulent eddies are much faster than those of the instability. This relaxes the constraints on minimum domain size concerning intrinsic length scales by Berger et al. [43].

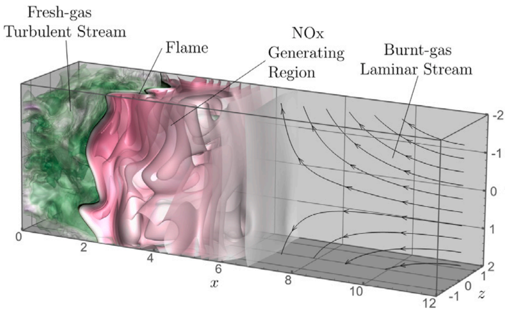

Fig. 1. Sketch of the DNS setup of turbulent counterflow premixed hydrogen flame under intensive strain. The dimensions are in millimetres [mm].

A turbulent stream of cold premixed reactants, with an average inflow velocity of $10\,\mathrm{m\,s^{-1}}$, enters the boundary located at $x = 0$. On this inflow boundary, homogeneous isotropic turbulence with an integral length scale of 1 mm and a root-mean-square (RMS) velocity of $4\,\mathrm{m\,s^{-1}}$ is superimposed using the digital-filter (DF) method [44] within a square region of size 3 × 3 mm at the centre of the domain boundary, resulting in a turbulent Reynolds number (Re) of 248.3, a Taylor length scale (l_λ) of 200 μm, and a Kolmogorov length scale η_K of 16 μm. On the opposite side, at $x = 12\,\mathrm{mm}$, a laminar stream of hot combustion products is introduced, with inflow velocities of $14\,\mathrm{m\,s^{-1}}$, $26\,\mathrm{m\,s^{-1}}$, and $50\,\mathrm{m\,s^{-1}}$, corresponding to bulk strain rates of $2000\,\mathrm{s^{-1}}$, $3000\,\mathrm{s^{-1}}$, and $5000\,\mathrm{s^{-1}}$, respectively. Variations in bulk strain rate are introduced solely by increasing the velocity of the hot product stream on the opposite side. This approach increases the momentum on the burnt-gas side, shifting the stagnation plane closer to the turbulent reactant side, thereby exposing the flame to a higher local strain without altering the imposed turbulence conditions. The product stream is kept laminar to minimize its impact on the turbulence field and to isolate the effects of strain. A similar methodology has been adopted in previous studies [41, 42,45]. For the two considered equivalence ratios, the temperature, pressure, and molar composition of the reactant and product streams are provided in Table 1. While temperature in combustion products boundary is set to match that of a free flame with the same equivalence ratio, its composition considers complete combustion, implying that only water vapour, nitrogen, and oxygen are present. While this setup is not feasible for laboratory testing, the complete combustion assumption is chosen to avoid initial NOx content, allowing the simulation to focus solely on NOx formation within the domain. The resulting turbulent and combustion regime conditions are summarized in Table 2. The turbulent Reynolds number based on the integral scales in our cases is below 2800, and the turbulent Karlovitz number $\mathrm{Ka_T}$ as defined in Table 2 is below 100, therefore the applied turbulence is moderate [46]. On the other hand, the Karlovitz number defined using the Kolmogorov length scale ($\mathrm{Ka_K}$) is about 627 and 436 for the equivalence ratios of 0.5 and 0.7, under which our cases for both equivalence ratios fall into the high-Karlovitz-number conditions according to the classification in [47]. It is worth noting that in the prescribed setup the in-flame and post-flame NOx levels are not diluted by the increased velocity of the products stream as the bulk strain is increased, neither by the effect of convection (streamlines from the products stream do not cross the stagnation plane) or diffusion, which can be verified by looking at the concentrations of water vapour in the flame as the bulk strain is increased (to be shown in the Results section). Therefore, all differences

Table 1

Temperature, pressure, and species mole fractions of the reactant-to-product counterflow test cases at different equivalence ratios.

	$\phi = 0.5$		$\phi = 0.7$	
	Reactants	Products	Reactants	Products
T	300 K	1640 K	300 K	2024 K
p	1 bar	1 bar	1 bar	1 bar
H_2	0.174	0.000	0.227	0.000
O_2	0.174	0.095	0.162	0.055
N_2	0.653	0.715	0.611	0.689
H_2O	0.000	0.190	0.000	0.256

Table 2

Flame parameters and conditions. The kinematic viscosity of air at 300 K, $\nu_0 = 1.6 \times 10^{-5}\ \mathrm{m^2\,s^{-1}}$, is used as a reference. The flame thickness δ is estimated using the unity flame Reynolds number [48]. Superscript 0 refers to unstretched conditions.

Parameters	$\phi = 0.5$	$\phi = 0.7$
δ_{th}^0 [μm]	400.2	333.8
s_L^0 [m s^{-1}]	0.568	1.409
$\delta = \nu_0/s_L^0$ [μm]	28.34	11.43
l_λ/δ	7.057	17.49
l_t/δ	35.28	87.48
u'/s_L^0	7.038	2.838
$Da = (l_t/\delta)(u'/s_L^0)^{-1}$	5.013	30.81
$Ka = (l_t/\delta)^{-1/2}(u'/s_L^0)^{3/2}$	3.143	0.511
$Re = Da^2 Ka^2 = u' l_t/\nu_0$	248.3	248.3
$Ka_{\mathrm{T}} = (l_t/\delta_{\mathrm{th}}^0)^{-1/2}(u'/s_L^0)^{3/2}$	11.81	2.76
$Ka_{\mathrm{K}} = (\delta_{\mathrm{th}}^0/\eta_k)^2$	626.6	436.1

in NOx (to be described in Section 4) are attributable to the direct effect of strain in the studied configuration.

The reacting compressible Navier–Stokes equations are solved with variable thermo-transport properties using a finite-rate chemistry model that includes 15 species and 37 elementary reaction steps, as discussed in the previous section. For all flame simulations, the computational domain is discretized using a grid of 576 × 192 × 144 cells, resulting in a grid spacing of 20 μm. Supplementary material includes the grid sensitivity study.

Boundary conditions are assigned as follows. The Digital Filter (DF) method of Laguarda and Hickel [44] is applied at the turbulent inflow boundary, on the $x = 0$-plane in Fig. 1. This method generates realistic synthetic turbulence with target spatial and temporal statistics. Temperature and density fluctuations are also set at the inflow boundary consistently with velocity fluctuations. At the laminar inflow boundary on the opposing x-plane, a non-reflecting boundary condition based on Riemann invariants is employed to eliminate reflections in the axial direction. A three-dimensional characteristic-based boundary condition is used at both outlet faces on the y-planes to prevent wave reflections and to maintain constant pressure as described in the Supplementary Material. Periodic boundary conditions are applied along the z-direction to facilitate statistical sampling.

All numerical simulations were conducted on the Dutch National Supercomputer Snellius. The wall clock time to simulate one flow-through time (FTT, ≈ 0.0012 s), including the time needed to write snapshots, is approximately 42 h on 12 nodes with two AMD Genoa 9654 CPUs (96 cores at 2.4 GHz per socket). The simulations are integrated for 10 FTT, which corresponds to approximately 1 million CPU hours for each test case.

4. Results and discussion

In this section, the turbulent flame topology is first discussed with the purpose of examining how different strain rates influence the overall flame structure under lean hydrogen–air conditions. The flame structure and emissions are then investigated in more detail to quantify the effects of turbulence and strain.

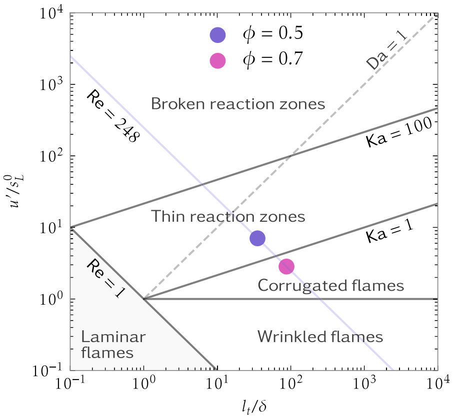

Fig. 2. Modified premixed combustion regime diagram [49] showing the simulation conditions. u' and l_t are the RMS velocity and integral length scale. s_L^0 is the laminar free flame speed and δ is the laminar flame thickness, calculated based on the unity flame Reynolds number [48].

Table 3

Variation of time averaged flame location (x_{fl}) and stagnation point (x_{st}) in the axial direction by increasing the bulk strain. Locations are reported in mm.

Strain	$\phi = 0.5$		$\phi = 0.7$	
	x_{fl}	x_{st}	x_{fl}	x_{st}
2000 s^{-1}	5.34 mm	7.47 mm	3.32 mm	7.02 mm
3000 s^{-1}	3.58 mm	5.50 mm	2.62 mm	5.38 mm
5000 s^{-1}	2.31 mm	3.46 mm	2.01 mm	3.73 mm

4.1. *Instantaneous reaction zone structure*

Both lean premixed configurations have the same turbulent velocity and length scale and, accordingly, the same turbulent Reynolds number of Re = 248. However, due to differences in their laminar flame speed — 0.568 m s^{-1} for $\phi = 0.5$ and 1.409 m s^{-1} for $\phi = 0.7$ at unstretched conditions — they exhibit different Damköhler and Karlovitz numbers. The flame conditions are found in the corrugated flamelets regime ($\phi = 0.7$) and the thin reaction zone regime ($\phi = 0.5$) of the Peters diagram [49], which is shown in Fig. 2. It is worth mentioning that this diagram refers to unstretched conditions.

The flame topology for equivalence ratio 0.5 is presented in Fig. 3 and for equivalence ratio 0.7 in Fig. 4, showing isolines of heat release rate in the mid y-plane at different levels of bulk strain. The turbulent stream of fresh gases enters the numerical domain from the left side and the laminar stream of hot combustion products enters from the right side. The root mean square (RMS) velocity of the turbulent motion significantly exceeds the flame propagation speed for all flame conditions. This results in pronounced wrinkling, corrugation, and curvature of the flame front, as seen in Figs. 3 and 4. When the bulk strain rate increases, the overall flame topology remains relatively unchanged for each equivalence ratio, as the turbulence conditions at the reactant inlet remain the same. Also, since the bulk strain is increased by increasing the flow rate of the hot product stream, the flame front moves leftward in the domain (towards the reactants stream). Simultaneously, the flame is getting closer to the stagnation plane, which also shifts leftward with increased strain, see Table 3 for details. Here, the flame location is defined as the location where the time-averaged water-based progress variable c becomes half, that is, $c \equiv Y_{\mathrm{H_2O}}/Y^b_{\mathrm{H_2O}} = 0.5$. The superscript b refers to the burnt conditions.

4.2. *Reaction zones structure in progress variable space*

To analyse the state–space structure of these turbulent flames, Fig. 5 presents scatter plots and conditional averages of major and minor

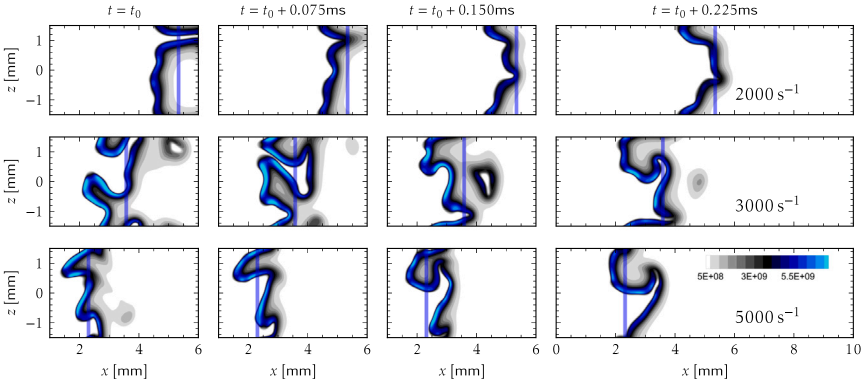

Fig. 3. Contours for different times, starting from a reference time t_0, of heat release rate (in W/m^2) at the midplane $y = 0$ for equivalence ratio of 0.5 and different bulk strain rates. The solid line shows the temporal-mean flame location.

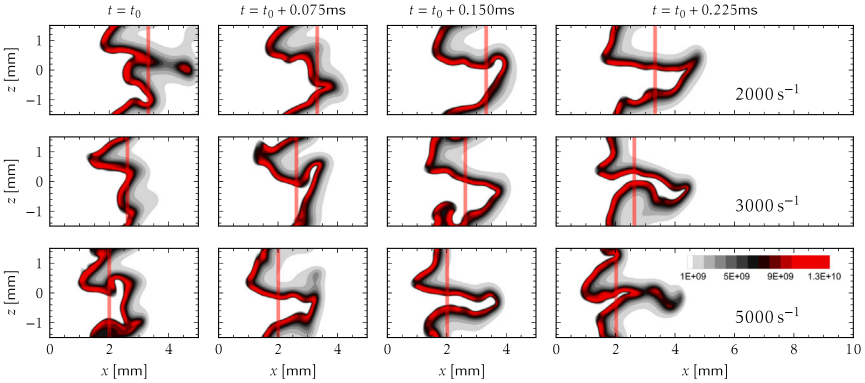

Fig. 4. Contours for different times, starting from a reference time t_0, of heat release rate (in W/m^2) at the midplane $y = 0$ for equivalence ratio of 0.7 and different bulk strain rates. The solid line shows the temporal-mean flame location.

species and heat release rate with respect to reduced temperature $\Theta \equiv (T - T^u)/(T^b - T^u)$, where superscripts u and b denote quantities of unburnt and burnt gas. Unconditioned scatter data, shown for the highest bulk strain rate, indicate that the reduced temperature can exceed unity for both equivalence ratios, confirming the transient presence of super-adiabatic regions within the turbulent flame. However, as will be shown for the discussion on the time-averaged profiles in Section 4.4.1, such regions are not sustained, which implies that turbulent mixing rapidly suppresses them through mixing with lower-temperature surroundings, in agreement with past studies [50,51]. To assess the effect of strain on this suppression, temperature probability density functions (PDFs) from the DNS in the post-flame region are further presented in Fig. 6 for two equivalence ratios. The figure shows that higher strain rates accelerate the suppression of super-adiabatic behaviour under similar turbulence conditions for both equivalence ratios. This may be due to the fact that generation of positive curvature due to thermodiffusive instabilities, which leads to super-adiabatic temperatures [52] is suppressed by the stablising, ‘pulling’ effect of bulk strain [6]. In fact, mean curvature is observed to become more and more negative as bulk strain increases for both the studied equivalence ratios (see Fig. 7, to be discussed later).

Looking at the profiles of the main species (H_2 and H_2O) in Fig. 5, it can be seen that these are not significantly affected by strain at either laminar or turbulent conditions, which is expected since the applied strain rates are relatively far from conditions of local extinctions of hydrogen flames and the turbulent Reynolds number is moderate. The fact that values of $\left\langle Y_{H_2O}|\Theta \right\rangle$ corresponding to values of $\Theta < 1$ remain unaffected by strain further indicates that the flame structure is not affected by dilution due to the higher flow rate of water vapour and air coming from the products stream as bulk stain increases, implying that changes in the distribution of minor species within the flame, to be discussed later, are a direct consequence of strain.

Moreover, the local behaviour of the major species across the turbulent flame front resembles that of laminar flames, except for an about 10% higher amount in mass fraction of hydrogen found for the turbulent case at low values of Θ (preheat zone). For a flat, positively strained, lean laminar hydrogen counterflow flame, molecular hydrogen moves towards the products faster than oxygen [21,53], causing a decrease of Bilger’s mixture fraction in the preheat region. This leaning effect is limited by positive strain [21], implying that a higher relative amount of fuel is found in the preheat region of the flame as strain increases. Since the bulk strain level for laminar and turbulent conditions is the same, the higher amount of hydrogen found in the preheat region at turbulent conditions could be due to the averaged affect of turbulent eddies, leading to an increase, on average, of tangential strain rate on the flame. This is indeed the case as can be observed in Fig. 7.

On the other hand, the increase of applied strain rate for a fixed condition (laminar or turbulent) does not seem to produce a significant variation of fuel mass fraction, suggesting that the limited leaning effect (or enhanced enriching effect) observed at turbulent conditions is instead more a consequence of turbulent eddies creating prevalently negative (concave towards the reactants) curvature. This is confirmed by the conditional average of flame curvature $(\nabla \cdot \mathbf{n}|\Theta)$ in Fig. 7, where $\mathbf{n}$ is the flame normal vector oriented towards the reactants. This result also aligns with what was observed in the DNS results of the slot burner configuration studied by Berger et al. [9], where prevalently negatively-curved flame fronts were observed for both thermodiffusively stable and unstable conditions (as for the flames presented here, as will be shown later), and a positive strain (due to the averaged effect of turbulent eddies) was observed on the flame. In the present work,

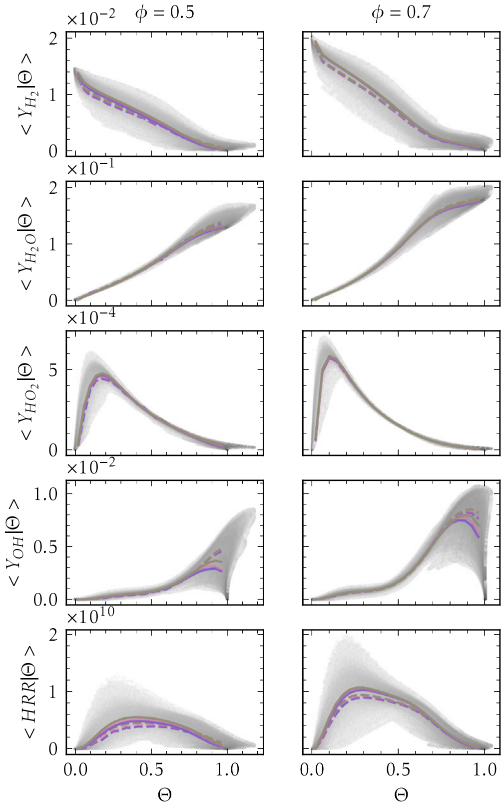

Fig. 5. Conditionally averaged species mass fractions and volumetric heat release rate in $[\mathrm{W\,m^{-3}}]$ versus reduced temperature (Θ) for two equivalence ratios and different bulk strains: 2000 $\mathrm{s^{-1}}$, 3000 $\mathrm{s^{-1}}$, and 5000 $\mathrm{s^{-1}}$. Solid lines refer to the turbulent conditions and dashed lines refer to the equivalent laminar conditions. The shaded area indicates scatter points of unconditioned values for the highest bulk strain rate case. (For interpretation of the references to colour in this figure legend, the reader is referred to the web version of this article.)

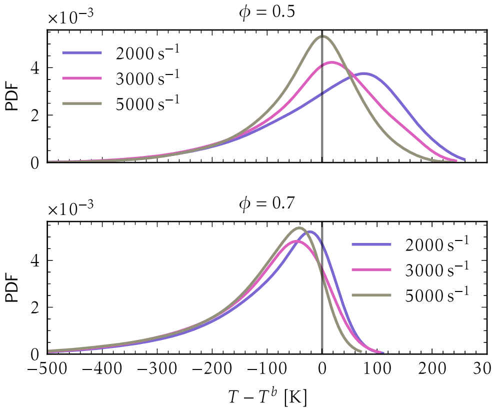

Fig. 6. Temperature distribution in the post-flame region for different bulk strains at two equivalence ratios. Statistics are collected for $0.95 < c_{\mathrm{H_2}} < 0.99$. The adiabatic flame temperature (T^b) is 1640 K and 2024 K for ϕ of 0.5 and 0.7.

however, positive tangential strain is produced by the combined effect of turbulent motion and intense applied strain rate in the counterflow configuration.

The effect of the mean applied strain rate becomes more evident by looking at the conditional average of heat release rate ($\mathrm{HRR} = \Sigma h_i \dot{\omega}_i$), which increases with applied strain for both laminar and turbulent conditions. Moreover, conditional values of HRR are higher at turbulent conditions for both equivalence ratio cases, except for high values of Θ. This is consistent with the previously discussed behaviour of local tangential strain, which is higher in the turbulent case due to the average effect of the turbulent eddies. This aspect is of particular interest in light of the observed NOx suppression at higher strain rate for laminar flames [20]. Since what ultimately determines the flame structure is the local tangential strain rather than the applied strain [54], this implies that the strain-induced NOx suppression might be enhanced in turbulent conditions. This aspect will be discussed further in Section 4.4. On the other hand, the relative increase of HRR at turbulent conditions as compared to laminar conditions seems markedly stronger at $\phi = 0.5$ as compared to the richer condition. This is believed to be due to a combination of the negative Markstein length at the lean condition and the fact that the prevalently negative curvature limits the effect of the overall stretch in enhancing the reaction rate. Berger et al. [9] showed that the vortex-enhanced tangential strain rate is prevalently due to the motion of small eddies, which are more strongly suppressed on average at the richer condition due to the higher heat release and adiabatic temperature. This balance between negative curvature and positive tangential strain plays more in favour of the former at higher equivalence ratios. It will be seen in the next section that this behaviour does not affect, however, the behaviour of NOx, which decreases with strain rate.

Regarding minor species, the conditional averages for the turbulent cases mostly exhibit an evolution similar to their laminar counterparts, indicating that turbulent eddies do not significantly affect the internal flame structures. Moreover, while radicals such as $\mathrm{HO_2}$ seem to remain unaffected by the increase of bulk strain and turbulence, the behaviour of OH radicals is observed to be significantly affected by both strain increase and turbulence level towards the burnt side of the flame, for both equivalence ratio conditions. As for the laminar condition, the peak of OH radicals increases with applied strain, which is consistent with the observations in Ref. [20]. This higher OH availability at higher strain will have an effect on NOx production, as will be discussed in Section 4.4. Nevertheless, the peak of OH is observed to be lower under turbulent conditions for the same applied strain rate level, and despite the additional tangential strain on the flame produced by the turbulent motion (see discussion above). This is partly explained by the fact that, unlike for laminar conditions, super-adiabatic temperatures are mitigated by turbulent mixing at the conditions studied here. This will be shown later in the discussion on emissions in Section 4.4. Moreover, it is not clear whether the additional strain yield by the local effect of a vortex on the flame lasts long enough to impart changes in the flame structure, which will be further investigated later in the paper.

4.3. *Curvature, strain and stretch evolution*

In order to highlight the effects of turbulence and applied strain on the internal structure and behaviour of the flame, Fig. 7 reports conditional averages as a function of the reduced temperature for: i) flame curvature $\nabla \cdot \mathbf{n}$, with $\mathbf{n} = -\nabla c/|\nabla c|$ being the flame normal vector and c being the progress variable based on the mass fraction of $\mathrm{H_2O}$; (ii) flame displacement speed $s_d = (1/|\nabla c|)Dc/Dt$; (iii) curvature rate $s_d \nabla \cdot \mathbf{n}$; (iv) tangential flame strain rate $a_t = \nabla \cdot \mathbf{u} - n_i S_{ij} n_j$, where $S_{ij} = (\partial u_i/\partial x_j + \partial u_j/\partial x_i)/2$ is the tensor element of the strain rate; and (v) flame stretch $\kappa = a_t + s_d \nabla \cdot n$. Following Ref. [55], Kolmogorov scales of length $\eta_K = 15.98\,\mu\mathrm{m}$, time $\tau_K = 158.7\,\mu\mathrm{s}$, and velocity $u_K = 0.101\,\mathrm{m/s}$ are used for non-dimensionalizing the results.

First, it is important to notice that the conditional tangential strain rate on the flame increases proportionally to the applied strain rate, in both laminar and turbulent conditions, by a significant amount, as intended. This was not straightforward since the applied strain rate is increased in the present setup by only increasing the velocity on the product side, while the flame is located on the reactants stream on the

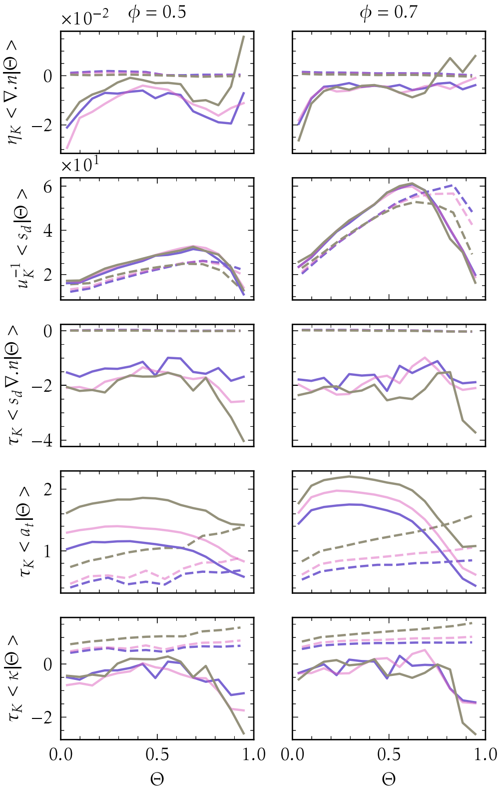

Fig. 7. Conditionally averaged flame curvature $\nabla.n$ [m^{-1}], displacement speed s_d, curvature rate $s_d\nabla.n$, tangential strain rate a_t, and stretch rate κ versus reduced temperature (Θ) at different bulk strains: 2000 s^{-1}, 3000 s^{-1}, and 5000 s^{-1}. Dashed lines show the laminar profiles. Kolmogorov scales are used for non-dimensionalizing the results. (For interpretation of the references to colour in this figure legend, the reader is referred to the web version of this article.)

other side of the stagnation plane, and thus not directly affected by the streamlines in the products stream.

Another observation is that turbulence produces a net average increase in strain as compared to the corresponding laminar cases, which is consistent with what was observed from DNS of hydrogen flames in a slot burner by Berger et al. [9]. This enhancing effect seems to decrease as moving towards higher values of Θ as one would expect since no turbulence is present on the products stream, resulting in an overall decreasing trend of a_t through the flame, in contrast to the laminar behaviour.

For $\Theta \rightarrow 1$ the conditional average of strain converges towards the laminar value for $\phi = 0.5$. For the case at $\phi = 0.7$, for $\Theta \rightarrow 1$ this does not seem to happen. However, this is not because laminar conditions are not being approached, but rather due to the fact that the turbulent flame accelerates towards the reactants due to the increase of flame surface, and thus towards regions with lower values of applied strain rate. This acceleration is proportionally weaker at the leaner equivalence ratio and therefore this effect is not markedly visible at the ultra-lean conditions.

Furthermore, for the same applied strain rate, the local flame-tangential strain rate is slightly smaller for the equivalence ratio of 0.5 as compared to 0.7 at both laminar and turbulent conditions, which is due to the fact that the flame is further away from the stagnation plane at the leaner condition, as can be inferred from Table 3, which provides the respective location of the stagnation plane and average flame location. The average flame location is defined as the point along the axial direction x where the time-averaged water-based progress variable is equal to half. Additionally, the stagnation point is identified where the time-averaged axial velocity is zero. This difference is more pronounced under turbulent conditions, indicating that the averaged strain-enhancing effect of turbulent eddies is somewhat stronger at higher equivalence ratios. This in turn may be related to the larger preheat region for the $\phi = 0.5$ case, which weakens the turbulent eddies before they impinge on the heat-releasing region, resulting in a weaker corrugation of the flame front, which is consistent with the observations in Figs. 3 and 4 and with the two flames belonging to different regimes of the modified Borghi diagram in Fig. 2.

Let us now look at the effect of applied strain rate on curvature. As one can observe from Fig. 7, curvature is on average negative across the flame front for both equivalence ratios, and weakly correlated with the applied strain rate. The curvature seems to reduce in absolute value with applied strain for the flame at $\phi = 0.5$, indicating that strain has a 'pulling' effect. On the other hand, this effect is not visible at the richer equivalence ratio. Also, what ultimately contributes to the stretch rate is the curvature rate (curvature multiplied by displacement speed), which is observed to exhibit the opposite trend, i.e., the curvature rate grows in absolute value as the applied strain rate increases. In order to understand this behaviour, one has to look into the effect of strain on the flame displacement speed, whose conditional average across the flame front is also reported in the figure.

By looking towards the unburnt side ($\Theta \rightarrow 0$), as commonly done to identify the displacement speed, one can notice a mild increase when passing from laminar to turbulent conditions, which is due to the on-average positive vortex-induced tangential strain rate. Nevertheless, an increase in bulk applied strain rate does seem to produce only a mild increase in displacement speed in the laminar case, and this increase is even weaker for turbulent conditions. Two observations are made at this point. First, the increase with applied strain rate of curvature rate (in absolute value), which seems in contrast to the behaviour observed for curvature and displacement speed, is a consequence of the fact that the latter two are not statistically independent, i.e., $E[XY] \neq E[X]E[Y]$, where $E[\circ]$ represents any defined expectation in a mathematical sense, and X and Y are random variables representing flame displacement speed and curvature in the present context. In fact, the flame displacement speed changes with curvature in hydrogen flames due to the coupling with differential diffusion [54]. Second, the flame displacement speed is not the most straightforward parameter to quantify the effect of strain for non-unity Lewis number mixtures, since the flame is also moving in space. For this purpose, the consumption speeds for both laminar and turbulent conditions are reported in Table 4.

The consumption speed is calculated here on the $y = 0$ plane and is based on the integral of the heat release rate, rather than the integral of the fuel burning rate [56], as $s_c = 1/[\rho^u(T^b - T^u)L_z] \iint \mathrm{HRR}/c_p\, dx\, dz$. This definition is proportional to the integral of the fuel reaction rate, which is in turn correlated with the heat release rate and thus, unlike displacement speed, must increase with the bulk strain rate at negative Markstein lengths $\mathcal{L} \equiv -(\partial s_c/\partial \kappa)|_{\kappa=0}$, consistent with the literature [53,54]. It is worth reiterating that the variation in Markstein length depends only on the strain rate under specific laminar conditions where the flame remains flat, while, as investigated in this work, curvature also affects $\mathcal{L}$ under turbulent conditions [57]. In general, the Markstein length associated with curvature is different from the value associated with strain, and this differentiation is not explicitly shown in the equation above for simplicity. By looking first at the values for the laminar flames, one can notice that the consumption speed increases with applied strain at the ultra-lean equivalence ratio and decreases at the richer condition. This is expected, since Markstein length changes sign from negative under ultra-lean conditions to positive at a critical equivalence ratio $\phi^* \approx 0.68$ [28]; therefore, the results reported in Table 4 suggest that the richer of the two conditions examined in the present study is above the critical value.

The behaviour of s_c for the turbulent condition is less obvious. For the turbulent cases at $\phi = 0.7$, the consumption speed decreases similarly to the laminar case. Note that the curvature rate is negative

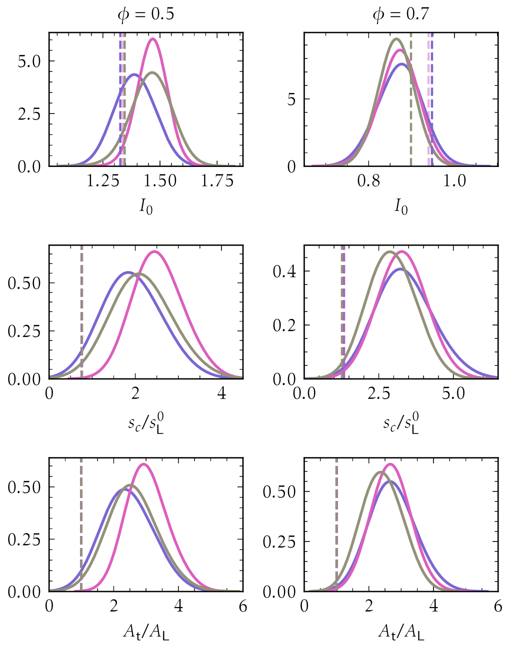

Fig. 8. Kernel density estimation (KDE) plots of the stretch index (I_0), ratio of consumption speed to free flame speed (s_c/s_L^0), and turbulent flame surface ratio (A_t/A_L) at different bulk strains: 2000 s^{-1}, 3000 s^{-1}, and 5000 s^{-1}. The dashed lines indicate the laminar counterparts for comparison. (For interpretation of the references to colour in this figure legend, the reader is referred to the web version of this article.)

on average, contributing thus to the overall value of s_c. Looking at the cases with $\phi = 0.5$, one can notice that, unlike the laminar case, the consumption speed only increases when the applied strain rate increases from $2000\,s^{-1}$ to $3000\,s^{-1}$, and then decreases again at $5000\,s^{-1}$. The reason for this is that the Markstein length is defined for zero stretch, but in reality, the stretch changes with strain. As strain increases, the consumption speed reaches a peak and then decreases again [54]. This peak occurs earlier at lower equivalence ratios. For the case at $\phi = 0.5$ this peak is at about $a = 4000\,s^{-1}$ (it can be estimated by laminar one-dimensional flamelet calculations for the same counterflow configuration proposed here, not shown), which is above the applied bulk value. However, in a turbulent condition, the additional mean strain induced by the turbulent motion shifts the effective applied strain value above the peak value, triggering the inversion of the Markstein length sign.

To distinguish between the relative effects of stretch and the increase in flame area on the consumption speed for turbulent cases, Fig. 8 shows the kernel density estimation (KDE) plot of the stretch index I_0, the consumption speed (normalized by the unstretched laminar flame speed) and the turbulent flame surface ratio A_t/A_L. The snapshot data used for the analysis were collected over a time window from 7 to 10 FTT. At each time step, the turbulent flame surface A_t is obtained by integrating the flame surface density across the whole domain as described in Refs. [58,59]. A_L is calculated as the cross-sectional area of the numerical domain. The stretch factor $I_0 = (s_c/s_L^0)/(A_t/A_L)$ quantifies the effect of the local variation of burning rate due to stretch. The laminar values are also shown in the figure as a reference. First, one can notice that I_0 is, respectively, above and below unity for the equivalence ratios of $\phi = 0.5$ and $\phi = 0.7$, meaning that the effect of strain increases the burning rate compared to the unstretched condition for $\phi = 0.5$ and decreases it for $\phi = 0.7$. This further indicates that even when the Markstein length changes sign at $a = 5000\ s^{-1}$ at $\phi = 0.5$, the consumption speed remains above the unstretched level; thus, the flame is still far from extinction.

Table 4
Variation of the laminar and turbulent consumption speed, s_c, by increasing the bulk strain at different equivalence ratios. Turbulent values are reported as temporal mean ± standard deviation.

	$\phi = 0.5$	
Strain	Laminar	Turbulent
$2000\,s^{-1}$	$0.75\ m\,s^{-1}$	$1.93 \pm 0.46\ m\,s^{-1}$
$3000\,s^{-1}$	$0.76\ m\,s^{-1}$	$2.53 \pm 0.39\ m\,s^{-1}$
$5000\,s^{-1}$	$0.77\ m\,s^{-1}$	$2.16 \pm 0.48\ m\,s^{-1}$
	$\phi = 0.7$	
Strain	Laminar	Turbulent
$2000\,s^{-1}$	$1.35\ m\,s^{-1}$	$3.36 \pm 0.64\ m\,s^{-1}$
$3000\,s^{-1}$	$1.34\ m\,s^{-1}$	$3.29 \pm 0.55\ m\,s^{-1}$
$5000\,s^{-1}$	$1.28\ m\,s^{-1}$	$2.94 \pm 0.55\ m\,s^{-1}$

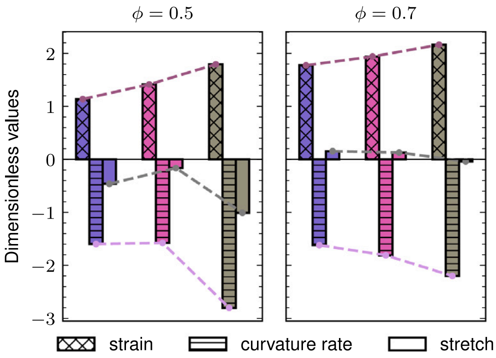

Fig. 9. Comparison of the conditional averages of strain, curvature rate, and stretch at the reduced temperature point where the heat release rate is maximum. Identical hatching marks the stretch components, while colour differentiates bulk strains: 2000 s^{-1}, 3000 s^{-1}, and 5000 s^{-1}. Dashed lines connect bar tops to show trends with the increase of the bulk strain rate. (For interpretation of the references to colour in this figure legend, the reader is referred to the web version of this article.)

The other observation is that at turbulent conditions the stretch effect on the flame speed is amplified at $\phi = 0.5$ and reduced at $\phi = 0.7$ as compared to the laminar case, which seems consistent with the fact that the mean positive tangential strain rate has increased at turbulent conditions. Note that the effect of the increase in area due to turbulence (wrinkling) is a rise in the consumption speed of a factor, on average, of approximately 2.7 and 2.5, respectively, for the cases at $\phi = 0.5$ and $\phi = 0.7$. However, for a fixed nominal equivalence ratio, the area increase remains about constant as the applied strain rate increases for the case at $\phi = 0.7$, and mildly increases and then decreases for the case at $\phi = 0.5$ (consistently with the observations for curvature in Fig. 7), thus indicating that the changes discussed for Table 4 are mainly attributable to the effect of stretch on the flame.

As a final remark, by looking at Fig. 7, one can notice that while the curvature rate becomes increasingly more negative as the applied strain rate is increased, the overall stretch rate, also reported in the figure, remains about constant for both equivalence ratios with negative or slightly positive values. This implies that at turbulent conditions, the negative curvature balances and overcomes the effect of the positive strain on the overall stretch rate. Nevertheless, as shown in Fig. 9, hydrogen flames respond differently to strain and curvature, leading to the definition of different Markstein lengths (e.g. see [60]), and according to the discussion above, the stretched hydrogen flame seems to respond more strongly to strain than to curvature. For the same reason, any changes in the flame structure (e.g., minor species behaviour and NOx formation to be discussed later) must be attributable to tangential strain rather than curvature. Flame-normal strain also does not have any major effect at the studied conditions since these flames are far from conditions of local extinctions, as discussed earlier.

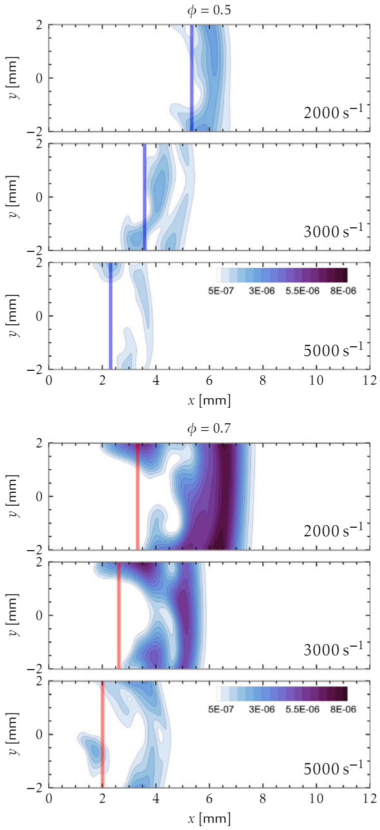

Fig. 10. Midplane contours of NO mass fractions plotted in the $z = 0$ plane at a random instant of time for different bulk strain rates and nominal equivalence ratios. The solid line marks the flame location.

4.4. Nitrogen oxides

Porcarelli et al. [20] found that NOx decreases overall due to the sole effect of increasing the applied strain rate in laminar counterflow flames. It was further noted that the suppression of NOx was prevalently due to a redistribution of OH radicals across the flame front. In particular, the overall suppression of NOx was observed to be mainly driven by the decrease of OH radical concentration in the downstream part of the flame, which overcompensated for the behaviour within the region of strong reactions, where both OH radical and NOx concentrations were observed to increase. Finally, it was observed that at negative Markstein length (ultra-lean conditions) the effect of overall suppression of NOx was limited by the increase of reactivity of the flame with strain, leading to super-adiabatic temperatures. In the present section, the effect of stretch on NOx formation is assessed at turbulent conditions. Our first objective is to assess whether the suppression of NOx is observed under turbulent conditions and how it compares to the laminar cases for the same applied strain. The second objective is to assess how the additional mean positive flame-tangential strain, existing due to the effect of turbulent motion, affects the NOx production. Finally, the effect of strain fluctuations will be investigated. Since NOx are slow-forming species, it is in fact unclear whether turbulence vortices can last long enough to affect the generation of NOx. Based on the discussion in the previous section, curvature effects will not be further assessed.

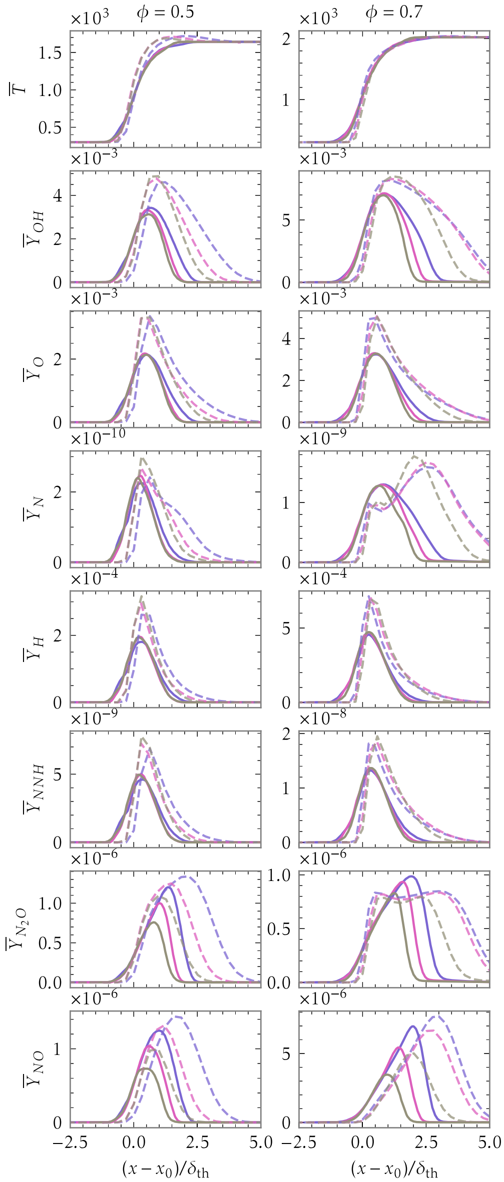

Fig. 11. Spatial variation of the time-averaged temperature and species mass fractions at different equivalence ratios and bulk strains: 2000 s^{-1}, 3000 s^{-1}, and 5000 s^{-1}. δ_{th} is the flame thermal thickness computed using time-averaged temperature profiles and x_0 is the position where the time-averaged water-based progress variable equals 0.5. The dashed lines indicate the laminar counterparts for comparison. (For interpretation of the references to colour in this figure legend, the reader is referred to the web version of this article.)

4.4.1. Post-flame and overall NOx suppression

In order to give a first impression of NOx formation under highly strained turbulent conditions, midplane contours of the NO mass fraction are shown in Fig. 10 for the two equivalence ratios and the three nominal bulk strain conditions. Due to the lower adiabatic flame temperature, flames with an equivalence ratio of 0.5 typically produce lower NO emissions compared to those with an equivalence ratio of 0.7, given identical bulk strain. As shown in the figure, the increase in the bulk strain reduces the peak levels of NO and confines the NOx generation to a smaller region for both equivalence ratios.

To understand how the flame structure is changing with increasing bulk strain level, time averages of NO and N_2O, as well as main radicals needed for NOx generation, are shown in Fig. 11. Profiles are plotted as a function of the flame-centred, flame-thickness-normalized longitudinal coordinate, effectively eliminating the influence of residence time on the results. The x-axis in the figure is therefore normalized with the thermal thickness of the flame calculated using the time averaged temperature profiles along the axial direction, $\delta_{th} \equiv (T^b - T^u)/\max(|\partial \mathrm{T}/\partial x|)$

Table 5

Variation of the laminar and time-averaged turbulent values of the density-weighted integral of NO, I_{NO} [$\mathrm{kg_{NO}/m}$]$\times 10^{12}$, with the bulk strain and equivalence ratios.

Bulk	$\phi = 0.5$		$\phi = 0.7$	
Strain	Laminar	Turbulent	Laminar	Turbulent
$2000\,\mathrm{s^{-1}}$	1.345	3.319	9.070	18.039
$3000\,\mathrm{s^{-1}}$	1.037	2.604	6.518	11.407
$5000\,\mathrm{s^{-1}}$	0.619	1.432	3.628	5.647

and adjusted to zero in the middle of the flame brush, identified here as the position x_0 where the time averaged water-based progress variable becomes half. This approach allows for a direct comparison of flame characteristics under different bulk strain rates and equivalence ratios, focusing purely on the intrinsic properties of the flame.

It is evident that, similar to previous findings for laminar cases [20], there is a notable decrease in NO and N_2O under turbulent conditions with bulk strain. Examining radical behaviour reveals that the decrease in NOx primarily results from the scarcity of radicals downstream of the flame ($x - x_0 > 0$), particularly OH, O, and N radicals, while H and NNH radicals appear to be less influential. Moreover, the reduction in radical concentration in the post-flame region with increased bulk strain is less strong at the lower equivalence ratio due to the limiting effect of the negative Markstein length in leaner conditions [20]. This results in a stronger percentage reduction of NO concentration in the case of $\phi = 0.7$, where the peak of NO mass fraction is reduced by almost 60 % by increasing the bulk strain rate from $2000\,\mathrm{s^{-1}}$ to $5000\,\mathrm{s^{-1}}$. Nevertheless, for the same increase of bulk strain, the suppression of peak NO mass fraction is also very significant at $\phi = 0.5$, with about 45 % reduction. Unlike the other species, N_2O is reduced more in percentage by the effect of increasing bulk strain at the ultra-lean condition, exhibiting a reduction of its peak by about 40 % when passing from the lowest to the highest imposed bulk strain, as compared to a reduction by about 20 % for the case at $\phi = 0.7$. This suggests that the reduction of NO with bulk strain occurs across different routes and, on the other hand, that the suppression via the N_2O route becomes more important as the flame becomes leaner. Note that the peak concentration of NNH radical shows a non-negligible increase with bulk strain at the leaner condition, indicating that, unlike the N_2O and thermal routes, the NNH route might increase NO with bulk strain due to the in-flame contribution. It is worth noting that the behaviour of NO discussed above is only related to that of intermediate radicals and not to temperature, whose values remain almost unaffected by the increase in bulk strain under turbulent conditions, as observed in Fig. 11. In other words, as the bulk strain increases, the flame thermal thickness shrinks. However, the reaction thickness of the radicals is reduced even more, preventing them from reaching the high-temperature zones where they would form the post-flame NOx.

So far, the results presented indicate that there is no large qualitative difference between the way NOx is suppressed at high strain in turbulent conditions compared to the laminar counterflow case investigated in Ref. [20]. To provide a quantitative comparison of the suppression potential under laminar and turbulent conditions, the density-weighted integral of NO at the two outlet boundaries along the y direction, calculated as $I_{NO} = \int_{\mathcal{A}} \rho Y_{NO}\, d\mathcal{A}$, is shown in Table 5. The instantaneous values of I_{NO} are further averaged in time for turbulent cases.

As shown in Table 5, the absolute values of I_{NO} are consistently higher in the turbulent flame due to the wrinkled flame surface. One can observe that I_{NO} at $\phi = 0.7$ reduces by about 28 % when increasing the applied strain from $2000\,\mathrm{s^{-1}}$ to $3000\,\mathrm{s^{-1}}$, and by 44 % for the strain increase from $3000\,\mathrm{s^{-1}}$ to $5000\,\mathrm{s^{-1}}$. The respective reduction of integral NO for the turbulent case are about 37 % and 50 %, i.e., the relative reduction is slightly stronger at turbulent conditions. By repeating the analysis at $\phi = 0.5$, one finds that I_{NO} reduces for the laminar condition by about 23 % and 40 % when increasing respectively the bulk applied strain from $2000\,\mathrm{s^{-1}}$ to $3000\,\mathrm{s^{-1}}$, and from $3000\,\mathrm{s^{-1}}$ to $5000\,\mathrm{s^{-1}}$. This reduction is milder than for the richer flame, which is consistent with the fact that NO is now increasing via the NNH route. The respective reductions of integral NO for the turbulent case at $\phi = 0.5$ are about 22 % and 45 %.

Some considerations are needed at this point. First, for leaner conditions, at least for the lower range of applied bulk strain, the reduction potential of NOx by strain at laminar and turbulent conditions becomes similar, which is believed to be due to the thermal route of NOx formation becoming less important at very lean conditions. This in turn implies that effects of super-adiabatic temperatures observed at laminar strained conditions is less important for the NOx generation in turbulent flow. On the other hand, when the applied bulk strain rate increases in the higher range, from $a = 3000\,\mathrm{s^{-1}}$ to $5000\,\mathrm{s^{-1}}$, the percentage reduction of integral NO for the turbulent $\phi = 0.5$ cases is again stronger than for the corresponding laminar cases. This is believed to be due to the fact that the effective mean tangential strain rate on the turbulent flame is higher than in laminar conditions, causing in this range of applied strain a transition from negative to positive Markstein length, as was discussed in Section 4.3. It is worth noting that, for the same reasons, the effective range of mean tangential strain on the turbulent flame is larger at turbulent conditions than at laminar conditions. Nevertheless, the absolute value of strain only determines the absolute value of NO integral (see for example Fig. 12 of [20]), while the potential of strain increase to suppress NOx is determined by the percentage increase of tangential strain applied to the flame. In this regard, it was shown analytically that I_{NO} scales as $I_{NO} \sim 1/a$ [20]. By looking at the conditional values of flame tangential strain in Fig. 7, one can notice that while the absolute increase of tangential strain on the flame is similar for laminar and turbulent condition, the percentage increase is lower for the turbulent flame due to the higher magnitude of tangential strain. Therefore, even considering the effective mean strain rate on the flame, the suppression potential of NOx at turbulent conditions would remain stronger than at laminar conditions. With the current DNS dataset it cannot be determined whether an increase of turbulence-driven strain rate at a fixed applied strain rate would result in a further decrease of I_{NO}, i.e. whether this component of mean tangential strain is as effective as the applied bulk strain rate. This analysis would require additional DNS data with different turbulence levels at the domain inlet. Nevertheless, it is shown in the present analysis that the turbulence-driven component has a beneficial effect in potentially shifting the flame response at high strain to positive Markstein length, resulting in a stronger NOx suppression process.

Overall, the analysis above indicates that NOx is suppressed faster at turbulent conditions compared to its laminar counterpart. It should be noted that this behaviour cannot be related to the turbulent flame area since it was shown in Fig. 8 that A_t is not affected by the bulk strain level imposed. The reasons for this stronger suppression of NOx at turbulent conditions have to be attributed to the in-flame NOx generation, which is investigated in the next section.

4.4.2. In-flame NOx

To describe the statistics at the flame surface, we use the generalized flame surface average approach based on the flame surface density (FSD) $\Sigma \equiv |\nabla c|$, with c being the progress variable defined based on the water mass fraction. While this is a common choice, it is known that using water mass fraction can introduce a bias in surface-based statistics due to its long tails in the burned gas side [61,62]. Since our analysis focuses on relative trends rather than absolute surface areas, the main conclusions remain unaffected by this choice. The FSD-averaged quantities further provide a detailed understanding of how the bulk strain and equivalence ratio influence the temperature and species concentrations that can contribute to NO production after the flame.

Table 6

Temporal mean values of the flame surface density (FSD) averaged quantities of species mass fractions over a time window from 7 to 10 times the flow-through time (FTT). Data are presented for different bulk strain rates and equivalence ratios.

Species	$\phi = 0.5$			$\phi = 0.7$		
	2000 s^{-1}	3000 s^{-1}	5000 s^{-1}	2000 s^{-1}	3000 s^{-1}	5000 s^{-1}
H	1.788e−04	2.007e−04	2.048e−04	4.471e−04	4.590e−04	4.673e−04
O_2	1.566e−01	1.579e−01	1.583e−01	1.312e−01	1.325e−01	1.357e−01
H_2O_2	3.218e−05	3.100e−05	2.769e−05	1.985e−05	2.006e−05	2.030e−05
HO_2	1.842e−04	1.949e−04	2.015e−04	1.710e−04	1.758e−04	1.869e−04
OH	1.716e−03	1.704e−03	1.700e−03	3.294e−03	3.226e−03	3.030e−03
O	1.485e−03	1.534e−03	1.539e−03	2.404e−03	2.414e−03	2.360e−03
H_2	4.665e−03	5.031e−03	5.294e−03	6.701e−03	6.941e−03	7.348e−03
H_2O	7.996e−02	7.811e−02	7.724e−02	1.049e−01	1.034e−01	1.000e−01
N_2	7.552e−01	7.553e−01	7.555e−01	7.508e−01	7.508e−01	7.509e−01
NO	4.183e−07	3.810e−07	3.671e−07	1.040e−06	9.141e−07	7.251e−07
N_2O	3.942e−07	3.542e−07	3.394e−07	3.906e−07	3.730e−07	3.407e−07
N	1.527e−10	1.741e−10	1.785e−10	6.654e−10	6.668e−10	6.470e−10
NH	1.335e−10	1.402e−10	1.420e−10	3.413e−10	3.404e−10	3.263e−10
NNH	3.400e−09	3.764e−09	3.852e−09	9.317e−09	9.531e−09	9.560e−09
NH_2	5.180e−11	5.463e−11	5.562e−11	1.059e−10	1.061e−10	1.033e−10

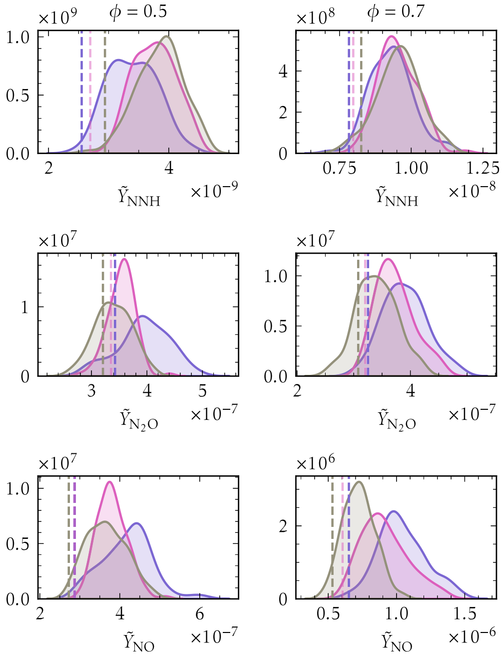

Fig. 12. Kernel density estimation (KDE) plots of the flame surface density (FSD) averages of NO, N_2O and NNH mass fractions at different equivalence ratios and bulk strains: 2000 s^{-1}, 3000 s^{-1}, and 5000 s^{-1}. The dashed lines indicate the laminar counterparts for comparison. (For interpretation of the references to colour in this figure legend, the reader is referred to the web version of this article.)

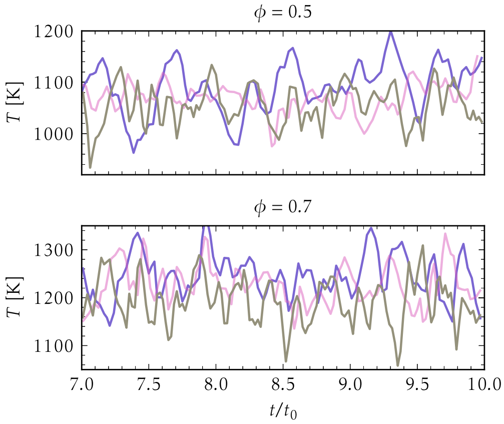

Fig. 13. Temporal variation of the flame surface density (FSD) averaged of temperature at different equivalence ratios and bulk strains: 2000 s^{-1}, 3000 s^{-1}, and 5000 s^{-1}. (For interpretation of the references to colour in this figure legend, the reader is referred to the web version of this article.)

The generalized FSD average of a quantity Q is calculated as $\tilde{Q} = \langle \Sigma Q \rangle / \langle \Sigma \rangle$, where the operator $\langle \cdot \rangle$ indicates the ensemble average at a given time step. Table 6 summarizes the temporal mean values of the FSD-averaged species mass fraction collected in the time interval 7 to 10 FTT for different bulk strain rates and equivalence ratios. The listed values reflect the local composition on the flame surface.

The FSD-averaged mass fractions of NO, N_2O, and NNH are complemented by KDE graphs in Fig. 12, which provide more detailed insights than temporal mean values alone by identifying the most probable concentrations and capturing the general distribution. Both the time-averaged values and the KDE plots demonstrate that in-flame NOx decreases with increasing bulk strain rate for both $\phi = 0.5$ and $\phi = 0.7$. The results indicate that, while NNH-derived NOx increases with strain, N_2O-derived NOx decreases, and combined with the thermal root, the net production of NOx is reduced under the applied turbulent conditions.

In-flame NOx levels are lower for $\phi = 0.5$, as expected since temperature is lower at the leaner condition which generally leads to reduced reaction rates and consequently lower NOx formation. Nevertheless, the change in flame temperature with increasing bulk strain is negligible for either equivalence ratio as shown in Fig. 13, highlighting that factors other than temperature, such as radical availability, play a more significant role in the NOx reduction.

By looking at the results in Table 6 and also considering the reaction path analysis obtained by tracking the oxygen atom discussed in Section 2, the observed reduction in N_2O-derived NOx with increasing strain rate can be related to the decreased concentration of OH radicals, which are essential for the conversion of N_2 to N_2O. In contrast, the increase in NNH-derived NOx is mainly associated with higher concentrations of H radicals, particularly under leaner conditions. This suggests that the shift in the radical pool directly influences the relative importance of the N_2O and NNH pathways in the formation of NOx.

Fig. 14 shows joint probability density functions (JPDFs) of FSD-averaged values of the mass fractions of NO, N_2O, and NNH and the actual flame-tangential strain. The JPDF contours highlight the most probable combinations and the correlation structure between these variables.

The horizontal axis shows the actual FSD-averaged flame-tangential strain rate. This value increases proportionally with the applied bulk

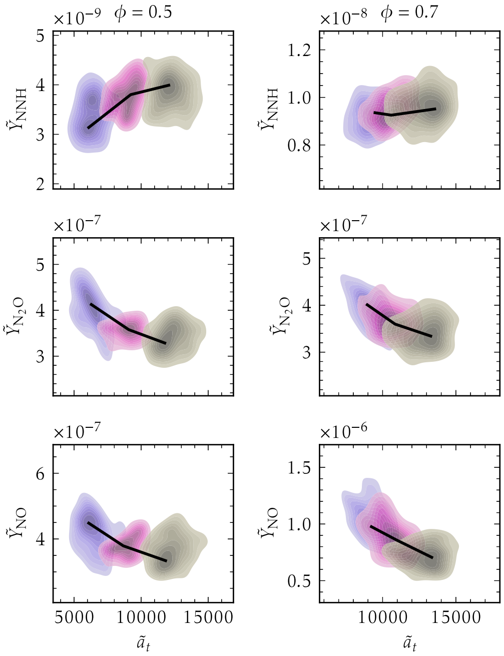

Fig. 14. Joint kernel density estimation (KDE) plot of flame-surface density averaged variables NO, N_2O and NNH mass fractions with the tangential flame strain rate a_t in [s^{-1}], at different equivalence ratios and bulk strains: 2000 s^{-1}, 3000 s^{-1}, and 5000 s^{-1}. (For interpretation of the references to colour in this figure legend, the reader is referred to the web version of this article.)

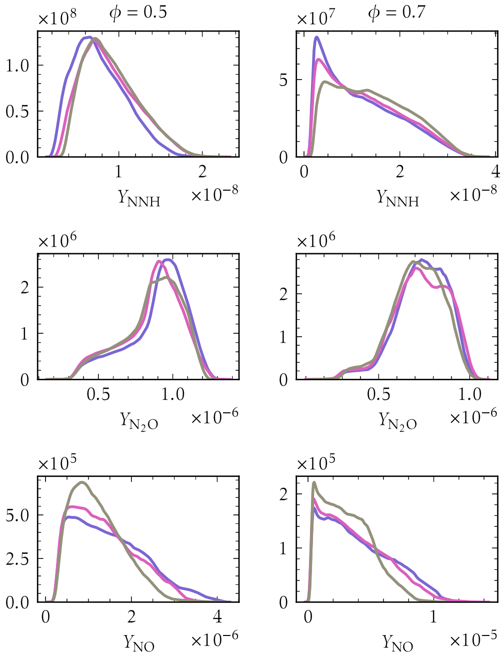

Fig. 15. Kernel density estimation (KDE) plots of NO, N_2O and NNH mass fractions for different nominal equivalence ratios and bulk strains: 2000 s^{-1}, 3000 s^{-1}, and 5000 s^{-1}. (For interpretation of the references to colour in this figure legend, the reader is referred to the web version of this article.)

strain, as one would expect. The main observation is the decrease in the NO mass fraction with increasing strain rates under turbulent conditions. By looking at the trends of the N_2O and NNH radicals, one can infer that while NNH generation is increased with the flame strain rate, N_2O contributes to the suppression of NO in the flame.

There are two competing effects within the flame, the first due to the tendency of the radicals needed for the formation of NOx to increase due to the strain-enhanced reactivity of the flame, and the second due to the redistribution of these radicals in a smaller region of space. At turbulent conditions the first effect is limited by the effect of turbulent mixing, which avoids the formation of super-adiabatic regions where the production of these radicals would be enhanced. As final observation, the rate of suppression of in-flame NO at turbulent conditions seems to be faster at the higher equivalence ratio, which is consistent with the fact that the Markstein length is positive at this condition [28].

4.4.3. *Effect of instantaneous strain*

In Section 4.4, it was shown that the time-averaged NOx levels consistently decrease with increasing bulk strain. However, due to turbulent fluctuations, instantaneous or local concentrations of NOx are not always lower at higher strain rates. It is thus useful to understand how these fluctuations affect the instantaneous NOx level.

In order to provide insight on how strongly turbulent fluctuations induce deviations from the mean (time averaged) values, probability density functions (PDFs) of NO, N_2O and NNH mass fractions are shown in Fig. 15, along with those for OH mass fraction and temperature. These PDFs have been constructed by sampling data from the entire computational domain at 12 uniformly spaced time instants over a statistically stationary period of 8 to 10 FTT. By looking at the behaviour of NO, one can notice that for both equivalence ratio cases the mode (most probable value) of the PDF remains about the same as the strain rate increases. Therefore, the overall decrease of NO seems to be dictated by the reduced probability of extreme values, i.e. data points located in the distribution tails at the right side. Similar observations can be made for N_2O, where the mode also remains about the same as the bulk strain increases. Differently than for NO, however, here the PDF is negatively skewed and the overall reduction of N_2O is due to events on the left side of the distribution (low values of Y_{N_2O}), and lower probability density at the opposite side. This redistribution is more marked at $\phi = 0.5$ and relatively mild at $\phi = 0.7$ in the case of N_2O, suggesting that this species significantly affect NO as strain increases only at very lean conditions. Different observations can be made for the NNH radical, which was already observed to increase with bulk strain at both equivalence ratio in the previous section. The results in Fig. 15 indicate that this increase with bulk strain for the flames at $\phi = 0.7$ is due to a higher occurrence of extreme values at the right tail (corresponding to increased positive skewness). On the contrary, for the flames at $\phi = 0.5$, the increase of NNH mass fraction with strain is due to an increase of the mode and a translation of the PDF towards higher values.

It would be interesting at this point to understand how the differences discussed above are related to the local values of tangential strain on the flame. For this purpose, mean conditional values with respect to the flame-tangential strain are shown in Fig. 16 for the NO, N_2O and NNH mass fraction. Values are collected throughout the flame front at different time instants. The data in the conditional plots is shown for the different datasets at different applied bulk strain separately, and also as an overall aggregate. One can notice that the decrease of NO mass fraction with tangential strain is not that obvious if one takes the datasets at different applied strain rates separately. On the other hand, the dependence on flame-tangential strain rate with decreasing trend of NO becomes very clear when the cases at different applied strain rate are combined. Similar considerations can be made for N_2O, although a mild decrease with a_t is clearly observed on the single datasets at $\phi = 0.5$. By also looking at the significant gap between regions of overlap in terms of tangential strain among datasets at different applied bulk strain rates, one can conclude that what matters to the reduction of NO and N_2O is the overall mean applied strain on the flame, while deviations from the mean value are only weakly correlated to the tangential strain. A different behaviour is observed for NNH, where

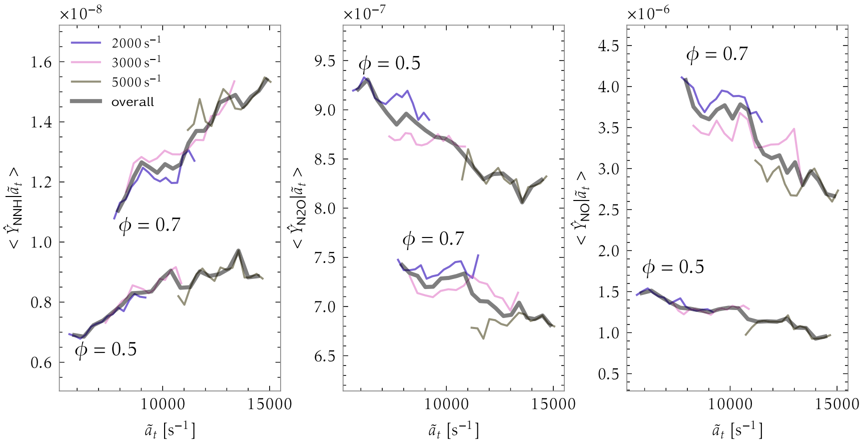

Fig. 16. Conditional mean of NO, N_2O and NNH mass fractions versus flame-tangential strain rate, for different nominal equivalence ratio and bulk applied strain levels. Aggregate overall values, obtained by considering the different cases at different applied bulk strain rates as a single dataset, are also shown.

Table 7
Pearson r values of NO fluctuations in its correlation to the FSD-averaged flame-tangential strain rate fluctuations for various bulk strains as presented in Fig. 17.

Strain	$\phi = 0.5$	$\phi = 0.7$
$2000\,s^{-1}$	−0.043	−0.349
$3000\,s^{-1}$	0.171	−0.242
$5000\,s^{-1}$	−0.229	−0.164

the results for all single datasets are close to the trend obtained by considering the data at different applied bulk strain altogether. This behaviour can be explained by the fact that NO is a slow-forming species and the values of tangential strain reported in Fig. 16 do not indicate anything about the time of permanence of a vortex on the flame front. In other words, the excess or defect of tangential strain on the flame compared to the overall mean, produced by the effect of a local vortex, might not last long enough to impart variations of NO. On the other hand, NNH is a much faster-forming species, which would explain the different observations for this radical.

An initial investigation of the effect of the fluctuating component of the tangential strain rate can be performed by plotting instantaneous data for FSD-averaged NO, N_2O and NNH mass fraction versus FSD-averaged flame-tangential strain, as shown in Fig. 17. Here the mean of the FSD-averages has been subtracted from the values to evaluate the effect of the fluctuating components only. Moreover, in-flame values have been considered since the time scale of formation of NO in this case is faster than post-flame NO, therefore this case is more conservative. If there was a strong influence on the tangential strain rate, these scatter plots should show some correlations between tangential strain rate and those species. By looking at the scatter plots in Fig. 17 and the correlation values (Pearson coefficients) in Table 7, one can notice that fluctuating values of in-flame NO are about uncorrelated to the corresponding fluctuations of tangential strain at $\phi = 0.5$, and this is independent of the bulk strain level considered. A stronger, but still weak, correlation is found for NO with a decreasing trend of the radicals as strain increases at $\phi = 0.7$, but this is not significant enough to suggest a correlated effect between instantaneous high tangential strain rate and lower NOx production. These results indicate that the NOx reduction mechanism is largely driven by bulk strain effects.

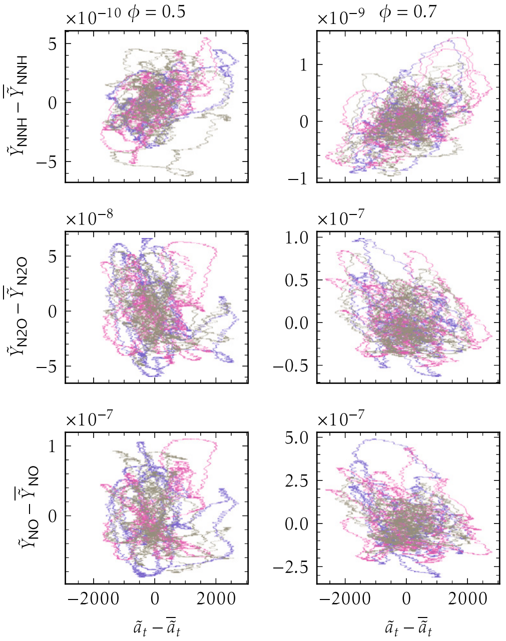

Fig. 17. Scatter plots of FSD-averaged NO, N_2O, and NNH mass fraction fluctuations versus fluctuations of FSD-averaged flame-tangential strain rate, for different nominal equivalence ratios and bulk strains: $2000\ s^{-1}$, $3000\ s^{-1}$, and $5000\ s^{-1}$. (For interpretation of the references to colour in this figure legend, the reader is referred to the web version of this article.)

5. Conclusions

Direct numerical simulations of hydrogen/air flames have been performed for increasing levels of applied strain on a turbulent reactants-to-products counterflow configuration to investigate how tangential strain affects the general flame behaviour and NOx emissions in particular. The analysis has been repeated for two lean equivalence ratios for which the Markstein length in the limit of low strain is respectively negative and positive.

It is found that the mean tangential strain on the flame causes a redistribution of radicals such as OH which result in an overall decrease of NO. This decrease with increased strain is found to be faster under turbulent conditions than for laminar flow. One reason for this is that turbulence limits the occurrences of super-adiabatic temperatures within the flame, thus limiting the in-flame NO production by the thermal route. Moreover, turbulence yields an effective increase of mean positive tangential flame on the flame which, unlike for the laminar case, triggers an inversion of the Markstein length at the highest strain rate from negative to positive in the leaner of the two configurations examined. Since a negative Markstein length is observed to limit the decrease of NOx, this inversion leads to a faster reduction of this species. Furthermore, the analysis conducted in the present study brought the following conclusions:

- overall NOx production within the domain mainly decreases due to the redistribution of radicals, in particular OH radicals. This decrease is primarily due to post-flame NOx, which always decreases with strain independently of the Markstein length;
- curvature does not seem to have a significant effect on the production of NO, despite its contribution to the overall stretch rate being significant as compared to that of strain;
- little correlation was found between the local fluctuations of flame-tangential strain rate and NOx production, which suggests the NOx reduction with high strain comes mostly from bulk effects.

The results mentioned above pertain to turbulent conditions characterized by moderate turbulent Reynolds numbers. They indicate that high levels of mean applied strain can be used to significantly suppress NOx emissions at practical combustor conditions, thus paving the way for the design of novel combustors based on this principle.

CRediT authorship contribution statement

Mohamad Fathi: Writing – original draft, Visualization, Validation, Software, Methodology, Investigation, Formal analysis, Conceptualization. **Stefan Hickel:** Writing – review & editing, Software, Methodology, Conceptualization. **Nguyen Anh Khoa Doan:** Writing – review & editing, Methodology, Conceptualization. **Ivan Langella:** Writing – review & editing, Project administration, Funding acquisition, Conceptualization.

Declaration of competing interest

The authors declare that they have no known competing financial interests or personal relationships that could have appeared to influence the work reported in this paper.

Acknowledgements

MF and IL acknowledge financial support from the ERC Starting Grant OTHERWISE, grant n. 101078821. The simulations have been performed at the Dutch National Supercomputer Snellius. The authors are grateful for the support of the SURF cooperative and the Dutch Research Council (NWO), grant n. 2023.044.

Appendix A. Supplementary data

Supplementary material related to this article can be found online at https://doi.org/10.1016/j.combustflame.2025.114459.

References

[1] S. Jensen, P. Larsen, M. Mogensen, Hydrogen and synthetic fuel production from renewable energy sources, Int. J. Hydrogen Energ. 32 (2007) 3253–3257.
[2] G. Leonard, J. Stegmaier, Development of an aeroderivative gas turbine dry low emissions combustion system, J. Eng. Gas Turbines Power 116 (1994) 542–546.
[3] T. Sattelmayer, W. Polifke, D. Winkler, K. Do'bbeling, NOx-abatement potential of lean-premixed GT combustors, J. Eng. Gas Turbines Power 120 (1998) 48–59.
[4] S. Ducruix, T. Schuller, D. Durox, S. Candel, Combustion dynamics and instabilities: elementary coupling and driving mechanisms, J. Propuls. Power 19 (2003) 722–734.
[5] J. O'Connor, V. Acharya, T. Lieuwen, Transverse combustion instabilities: acoustic, fluid mechanic, and flame processes, Prog. Energy Combust. Sci. 49 (2015) 1–39.
[6] G.I. Sivashinsky, C.K. Law, G. Joulin, On stability of premixed flames in stagnation-point flow, Combust. Sci. Technol. 28 (1982) 155–159.
[7] C.E. Frouzakis, N. Fogla, A.G. Tomboulides, C. Altantzis, M. Matalon, Numerical study of unstable hydrogen/air flames: shape and propagation speed, Proc. Combust. Inst. 35 (2015) 1087–1095.
[8] P.E. Lapenna, G. Troiani, F. D'Alessio, F. Creta, Synergistic interplay of thermodiffusive instability and turbulence in premixed flames, Proc. Combust. Inst. 40 (2024) 105499.
[9] L. Berger, A. Attili, H. Pitsch, Synergistic interactions of thermodiffusive instabilities and turbulence in lean hydrogen flames, Combust. Flame 244 (2022) 112254.
[10] A. Sahu, R. Ravikrishna, Quantitative LIF measurements and kinetics assessment of NO formation in H2/CO syngas–air counterflow diffusion flames, Combust. Flame 173 (2016) 208–228.
[11] N. Samiran, C. Chong, J. Ng, M. Tran, H. Ong, A. Valera-Medina, W. Chong, M. Nazri, Experimental and numerical studies on the premixed syngas swirl flames in a model combustor, Int. J. Hydrogen Energ. 44 (2019) 24126–24139.
[12] B. Fumey, T. Buetler, U. Vogt, Ultra-low NOx emissions from catalytic hydrogen combustion, Applied Energy 213 (2018) 334–342.
[13] S. Hernandez, Q. Wang, V. McDonell, A. Mansour, E. Steinthorsson, B. Hollon, Micro mixing fuel injectors for low emissions hydrogen combustion, in: Turbo Expo: Power for Land, Sea, and Air, vol. 43130, 2008, pp. 675–685.
[14] M. Kotob, T. Lu, S. Wahid, Experimental comparison between steam and water tilt-angle injection effects on NOx reduction from the gaseous flame, RSC Adv. 11 (2021) 25575–25585.
[15] H. Magnes, S. Marragou, A. Aniello, L. Selle, T. Poinsot, T. Schuller, Impact of preheating on flame stabilization and NOx emissions from a dual swirl hydrogen injector, J. Eng. Gas Turbines Power 146 (2024).
[16] A. De, S. Acharya, Parametric study of upstream flame propagation in hydrogen-enriched premixed combustion: effects of swirl, geometry and premixedness, Int. J. Hydrogen Energ. 37 (2012) 14649–14668.
[17] J. Chen, H. Im, Stretch effects on the burning velocity of turbulent premixed hydrogen/air flames, Proc. Combust. Inst. 28 (2000) 211–218.
[18] F. Vance, Y. Shoshin, L. de Goey, J. van Oijen, Quantifying the impact of heat loss, stretch and preferential diffusion effects to the anchoring of bluff body stabilized premixed flames, Combust. Flame 237 (2022) 111729.
[19] Y. Marzouk, R. Speth, A. Ghoniem, Combined Effects of Curvature and Strain on Hydrogen Enriched Lean Methane Flames, Tech. rep., Sandia National Lab.(SNL-CA), Livermore, CA (United States), 2005.
[20] A. Porcarelli, B. Kruljević, I. Langella, Suppression of NOx emissions by intensive strain in lean premixed hydrogen flamelets, Int. J. Hydrogen Energ. 49 (2024) 413–431.
[21] A. Porcarelli, I. Langella, Mitigation of preferential diffusion effects by intensive strain in lean premixed hydrogen flamelets, Proc. Combust. Inst. 40 (2024) 105728.
[22] C. Yoo, Y. Wang, A. Trouvé, H. Im, Characteristic boundary conditions for direct simulations of turbulent counterflow flames, Combust. Theory Model. 9 (2005) 617–646.
[23] C. Yoo, H. Im, Characteristic boundary conditions for simulations of compressible reacting flows with multi-dimensional, viscous and reaction effects, Combust. Theory Model. 11 (2007) 259–286.
[24] T. Capurso, D. Laera, E. Riber, B. Cuenot, NOx pathways in lean partially premixed swirling H2-air turbulent flame, Combust. Flame 248 (2023) 112581.
[25] A. Purohit, A. Nalbandyan, P. Malte, I. Novosselov, NNH mechanism in low-NOx hydrogen combustion: experimental and numerical analysis of formation pathways, Fuel 292 (2021) 120186.
[26] X. Wen, L. Berger, L. Cai, A. Parente, H. Pitsch, Thermodiffusively unstable laminar hydrogen flame in a sufficiently large 3d computational domain–part ii: nox formation mechanism and flamelet modeling, Combust. Flame 265 (2024) 113497.
[27] X. Wen, L. Berger, A. Scholtissek, A. Parente, C. Hasse, H. Pitsch, Numerical analysis and flamelet modeling of nox formation in a thermodiffusively unstable premixed hydrogen flame at elevated-pressure conditions, Proc. Combust. Inst. 40 (2024) 105411.
[28] M. Acquaviva, A. Porcarelli, I. Langella, Influence of Soret effect on flame structure and NOx emissions in highly strained lean premixed counterflow hydrogen flames, Fuel 395 (2025) 134939.
[29] M. Fathi, S. Hickel, D. Roekaerts, Large eddy simulations of transcritical e-fuel sprays using real-fluid multiphase flamelet-based modeling, Combust. Flame 281 (2025) 114360.
[30] M. Fathi, S. Hickel, D. Roekaerts, Large eddy simulations of reacting and non-reacting transcritical fuel sprays using multiphase thermodynamics, Phys. Fluids 34 (2022).
[31] L. Laguarda, S. Hickel, F. Schrijer, B. Van Oudheusden, Reynolds number effects in shock-wave/turbulent boundary-layer interactions, J. Fluid Mech. 989 (2024) A20.
[32] W. Wu, L. Laguarda, D. Modesti, S. Hickel, Passive control of shock-wave/turbulent boundary-layer interaction using spanwise heterogeneous roughness, Flow Turbul. Combust. (2024) 1–21.
[33] M. Fathi, D. Roekaerts, S. Hickel, Numerical simulation of transcritical multiphase combustion using real-fluid thermochemical and transport properties, Combust. Flame 275 (2025) 114055.
[34] G. Strang, On the construction and comparison of difference schemes, SIAM J. Numer. Anal. 5 (1968) 506–517.

[35] Y. Morii, H. Terashima, M. Koshi, T. Shimizu, E. Shima, ERENA: A fast and robust Jacobian-free integration method for ordinary differential equations of chemical kinetics, J. Comput. Phys. 322 (2016) 547–558.
[36] S. Hickel, C. Egerer, J. Larsson, Subgrid-scale modeling for implicit large eddy simulation of compressible flows and shock-turbulence interaction, Phys. Fluids 26 (2014) 106101.
[37] S. Gottlieb, C. Shu, Total variation diminishing Runge-Kutta schemes, Math. Comput. 67 (1998) 73–85.
[38] A. Sánchez, F. Williams, Recent advances in understanding of flammability characteristics of hydrogen, Prog. Energy Combust. Sci. 41 (2014) 1–55.
[39] A. Ern, V. Giovangigli, Impact of detailed multicomponent transport on planar and counterflow hydrogen/air and methane/air flames, Combust. Sci. Technol. 149 (1999) 157–181.
[40] M.X. Yao, G. Blanquart, Isolating effects of large and small scale turbulence on thermodiffusively unstable premixed hydrogen flames, Combust. Flame 269 (2024) 113657.
[41] S. Lyra, H. Kolla, B. Coriton, A. Gomez, J. Frank, J. Chen, Extinction of stratified counterflow H2/air premixed flames under intense turbulence and strain, in: 8th US National Combustion Meeting, 2013, pp. 3448–3458.
[42] Z. Jozefik, A.R. Kerstein, H. Schmidt, S. Lyra, H. Kolla, J.H. Chen, One-dimensional turbulence modeling of a turbulent counterflow flame with comparison to dns, Combust. Flame 162 (8) (2015) 2999–3015.
[43] L. Berger, K. Kleinheinz, A. Attili, H. Pitsch, Characteristic patterns of thermodiffusively unstable premixed lean hydrogen flames, Proc. Combust. Inst. 37 (2019) 1879–1886.
[44] L. Laguarda, S. Hickel, Analysis of improved digital filter inflow generation methods for compressible turbulent boundary layers, Comput. Fluids 268 (2024) 106105.
[45] B. Coriton, J.H. Frank, A. Gomez, Effects of strain rate, turbulence, reactant stoichiometry and heat losses on the interaction of turbulent premixed flames with stoichiometric counterflowing combustion products, Combust. Flame 160 (2013) 2442–2456.
[46] J.F. Driscoll, J.H. Chen, A.W. Skiba, C.D. Carter, E.R. Hawkes, H. Wang, Premixed flames subjected to extreme turbulence: some questions and recent answers, Prog. Energy Combust. Sci. 76 (2020).
[47] L. Berger, A. Attili, M. Gauding, H. Pitsch, Effects of karlovitz number variations on thermodiffusive instabilities in lean turbulent hydrogen jet flames, Proc. Combust. Inst. 40 (2024) 105219.
[48] T. Poinsot, D. Veynante, Theoretical and numerical combustion, RT Edwards, Inc., 2012.
[49] N. Peters, The turbulent burning velocity for large-scale and small-scale turbulence, J. Fluid Mech. 384 (1999) 107–132.
[50] V. Kuznetsov, Influence of turbulence on the formation of high nonequilibrium concentrations of atoms and free radicals in diffusion flames, Fluid Dynamics 17 (1982) 815–820.
[51] A.J. Aspden, M.S. Day, J.B. Bell, Towards the distributed burning regime in turbulent premixed flames, J. Fluid Mech. 871 (2019) 1–21.
[52] A.J. Aspden, M.S. Day, J.B. Bell, Turbulence–flame interactions in lean premixed hydrogen: transition to the distributed burning regime, J. Fluid Mech. 680 (2011) 287–320.
[53] J. van Oijen, A. Donini, R. Bastiaans, R. Thije Boonkkamp, P. de Goey, State-of-the-art in premixed combustion modeling using flamelet generated manifolds, Prog. Energy Combust. Sci. 57 (2016) 30–74.
[54] C. Law, Dynamics of stretched flames, Proc. Combust. Inst. 22 (1989) 1381–1402.
[55] S. Luca, A. Attili, E.L. Schiavo, F. Creta, F. Bisetti, On the statistics of flame stretch in turbulent premixed jet flames in the thin reaction zone regime at varying reynolds number, Proc. Combust. Inst. 37 (2019) 2451–2459.
[56] Y.-C. Chen, M. Kim, J. Han, S. Yun, Y. Yoon, Measurements of the heat release rate integral in turbulent premixed stagnation flames with particle image velocimetry, Combust. Flame 154 (2008) 434–447.
[57] D. Bradley, P. Gaskell, X. Gu, Burning velocities, markstein lengths, and flame quenching for spherical methane-air flames: a computational study, Combust. Flame 104 (1996) 176–198.
[58] L. Vervisch, E. Bidaux, K. Bray, W. Kollmann, Surface density function in premixed turbulent combustion modeling, similarities between probability density function and flame surface approaches, Phys. Fluids 7 (1995) 2496 – 2503.
[59] J. Gaucherand, D. Laera, C. Schulze-Netzer, T. Poinsot, DNS of turbulent premixed ammonia/hydrogen flames: the impact of thermo-diffusive effects, Flow Turbul Combust. 112 (2024) 587–614.
[60] T. Chen, S. Yu, Y.C. Liu, Flow strain and curvature markstein numbers of edge flame in the counterflow configuration, Int. J. Hydrogen Energ. 48 (2023) 10692–10700.
[61] T. Howarth, A. Aspden, An empirical characteristic scaling model for freely-propagating lean premixed hydrogen flames, Combust. Flame 237 (2022) 111805.
[62] L. Berger, A. Attili, H. Pitsch, Intrinsic instabilities in premixed hydrogen flames: parametric variation of pressure, equivalence ratio, and temperature. part 2–non-linear regime and flame speed enhancement, Combust. Flame 240 (2022) 111936.